Journal of Materials Chemistry A

ROYAL SOCIETY OF CHEMISTRY

PAPER

View Article Online
View Journal | View Issue

Cite this: J. Mater. Chem. A, 2021, 9, 17434

A multifunctional covalently linked graphene–MOF hybrid as an effective chemiresistive gas sensor†

Kolleboyina Jayaramulu, ‡*[ae] Marilyn Esclance DMello, †[b] Kamali Kesavan, [cj] Andreas Schneemann, [d] Michal Otyepka, [eh] Stepan Kment, [ei] Chandrabhas Narayana, [ck] Suresh Babu Kalidindi, [f] Rajender S. Varma, [e] Radek Zboril [ehi] and Roland A. Fischer *[g]

A hybrid of GA@UiO-66-NH_2 was synthesized based on the covalent assembly of graphene acid (GA) and the amine functionalized UiO-66 metal–organic framework through amide bonds. This strategy endows the material with unique properties, such as hierarchical pores, a porous conductive network decorated with functional groups, a high specific surface area, and a good chemical and thermal stability. The resultant hybrid has an electrical resistance of $\sim 10^4$ Ω, whereas the pristine GA and UiO-66-NH_2 possess an electrical resistance of $\sim 10^2$ Ω and $\sim 10^9$ Ω, respectively. The hybrid GA@UiO-66-NH_2 was demonstrated for CO_2 chemiresistive sensing and displayed a very fast response and quick recovery time of ~18 s for 100% CO_2, at 200 °C. While the pristine GA exhibits negligible response under the same conditions, GA@UiO-66-NH_2 exhibited a response of 10 ± 0.6%. Further, *in situ* temperature dependent Raman studies during CO_2 exposure confirm the presence of strong hydrogen bonding interaction between CO_2 and the amide functionality present on GA@UiO-66-NH_2. The resulting gas sensing characteristics of GA@UiO-66-NH_2 are majorly attributed to the better interaction of CO_2 at the amide/amine functional groups and the readily accessible hierarchical pores. This design strategy opens new horizons in the development of covalently linked hybrids with hierarchical porous conductive networks which can help to improve the gas sensing properties of MOF-based materials.

Received 18th April 2021
Accepted 22nd July 2021

DOI: 10.1039/d1ta03246a

rsc.li/materials-a

1. Introduction

The detection of CO_2 *via* chemiresistive technology has a huge commercial potential, since it is a very sensitive marker for human activity.[1–3] From the CO_2 concentration in the atmosphere of closed rooms and buildings, the occupancy by people can be determined.[4] This can be used to predict and prevent events related to overcrowding of areas, which ultimately can lead to disasters. Also, CO_2 detection can be used by rescuers after earthquakes or similar incidents to detect survivors that are trapped under the rubble of collapsed structures.[5] Current technologies detect CO_2 based on non-dispersive IR optical sensors.[6] Even though these sensors are well established, they still have some drawbacks, including their complexity, cost, scalability, and energy consumption. Chemiresistive sensing is a good alternative to the currently used detection methods.[7–15] Upon an outer stimulus, these sensors rely on changes in electrical resistance, that allow continuous monitoring of

[a]Department of Chemistry, Indian Institute of Technology Jammu, Jammu & Kashmir, 181221, India. E-mail: jayaramulu.kolleboyina@iitjammu.ac.in; jayaram72@gmail.com
[b]Materials Science and Catalysis Division, Poornaprajna Institute of Scientific Research, Devanahalli, Bengaluru, 562164, India
[c]Chemistry and Physics of Materials Unit, Jawaharlal Nehru Centre for Advanced Scientific Research (JNCASR), Jakkur, Bangalore, 560064, India
[d]Lehrstuhl für Anorganische Chemie I, Technische Universität Dresden, Bergstr. 66, 01069 Dresden, Germany
[e]Regional Centre of Advanced Technologies and Materials, Czech Advanced Technology and Research Institute, Palacký University Olomouc, Šlechtitelů 27, 783 71 Olomouc, Czech Republic
[f]Department of Inorganic and Analytical Chemistry, Andhra University, Visakhapatnam, 530 003, India
[g]Chair of Inorganic and Metal-Organic Chemistry, Department of Chemistry and Catalysis Research Centre, Technical University of Munich, 85748 Garching, Germany. E-mail: roland.fischer@tum.de
[h]IT4Innovations, VSB – Technical University of Ostrava, 17. listopadu 2172/15, 708 00 Ostrava-Poruba, Czech Republic
[i]Nanotechnology Centre, Centre of Energy and Environmental Technologies, VŠB–Technical University of Ostrava, 17, listopadu 2172/15, 708 00 Ostrava-Poruba, Czech Republic
[j]Central Characterisation Department, CSIR- Institute of Minerals and Materials Technology, Bhubaneswar, Odisha, India
[k]Rajiv Gandhi Centre for Biotechnology Thycaud P.O., Poojappura Thiruananthapuram, India

† Electronic supplementary information (ESI) available: Tables S1 and S2, general characterization details, gas sensing measurements setup and additional data on Raman spectroscopy. See DOI: 10.1039/d1ta03246a

‡ K. J. and M. E. D. contributed equally to this work.

various gas concentrations. One of the most critical challenges in the development of CO_2 gas sensors is the inclusion of active sites for adsorption/desorption, where CO_2 gas can cause changes in electrical parameters. Some nanostructured metal oxides, conducting polymers and other carbon-based materials have been considered as active materials in chemiresistive CO_2 gas sensors.[16–22] Among these, amine functionalized graphene and polymer materials are regarded as attractive materials with the capability of low concentration detection with high sensitivity and selectivity under ambient conditions.[19,23–28] However, these amine-based composite sensors display sharply decreasing sensitivity with reduced interactions over time. Hence, the need for the modifications of the active species over graphene-based materials to improve the signal-transducer interaction is essential for CO_2 sensing.

Metal–organic frameworks (MOFs), as a class of porous materials have various potential applications in the field of energy storage and conversion and also a lot of efforts have been made in the development of MOF-based sensors.[29–33] In particular, conjugated layered two-dimensional (2D) MOFs have recently been demonstrated as attractive CO_2 gas sensors by combining the desired properties of conductivity, nano porosity and the presence of functional groups for analyte adsorption.[11,12,34] However, their response and recovery times are still limiting their potential application. Although many pristine MOFs have conductivity limitations (mostly near insulators), there are some examples of conductive 2D layered MOF structures.[35] Several efforts have been made to improve the conductivity of three dimensional (3D) MOFs, for instance by hybridization with other conducting/semiconducting materials such as metal oxide nanoparticles, quantum dots, polymers, or carbon based materials.[36–44] In recent years, our groups demonstrated the noncovalent and covalent hybridization of MOFs with graphene to prepare conductive materials for various energy applications.[33,45–48] In particular, the covalent linking of graphene with appropriately functionalized MOFs has shown promising electronic properties for energy applications. Additionally, the strong bonding between each of the pristine components, the hierarchical pore architecture, and the enhanced thermal and chemical stabilities are all features which are sought after for the development of robust chemiresistive sensors.

Herein, we report the use of a covalently assembled hybrid constructed from graphene acid (GA) and amine functionalized UiO-66-NH_2 ($Zr_6O_4(OH)_4(NH_2\text{-bdc})_6$ with $NH_2\text{-bdc}^{2-}$ = 2-amino-1,4-benzenedicarboxylate)[49–53] for chemiresistive CO_2 sensing. In the material, UiO-66-NH_2 is covalently bound with GA *via* amide bonds, creating the hybrid GA@UiO-66-NH_2 (Fig. 1). The material shows hierarchical porosity, wherein the micropores are located at the octahedral UiO-66-NH_2 nanocrystals and the mesopores are built up through the stacking of GA through the MOF nanocrystals. The hierarchical architecture facilitates gas diffusion through the material, hence providing faster access to the interaction sites for the analytes. On the other hand, the interconnected conductive network ensures quick readout of the signal. In comparison, graphene has a low electrical resistance ($\sim 10^{-6}$ Ω) and high carrier electron mobility, but the lack of specific and strong interaction sites for the adsorption of gaseous analytes, renders it unusable for chemiresistive sensing in its pristine form. Here, the resultant hybrid GA@UiO-66-NH_2 provides interaction sites at the amide linkages present at the interface of graphene and the MOF for detectable change in resistance upon CO_2 interaction. These results are clarified by temperature dependent *in situ* Raman spectroscopy during exposure of the material to CO_2. In this study, a good correlation has been achieved between sensing characteristics and the novel functional properties obtained after integrating the MOF with graphene.

2. Experimental section

2.1. Synthesis of graphene acid

Graphene acid was prepared according to the literature.[31] To prepare graphene acid, the commercial fluorinated graphite (120 mg) was sonicated in presence of 15 mL of *N*,*N*-dimethylformamide (DMF) for 4 h under nitrogen atmosphere in a 25 mL round-bottom flask. To this mixture, 800 mg sodium cyanide (NaCN) was added and the mixture was heated to 130 °C with a condenser under stirring (500 rpm) for 24 h. During the reaction procedure, the intermediate and final product were cooled to room temperature, after which an equal amount of acetone was added. The materials were then separated by centrifugation and further purified by successive washing steps using DMF, dichloromethane, acetone, ethanol and water (each step was repeated four times). Additionally, hot (80 °C) DMF

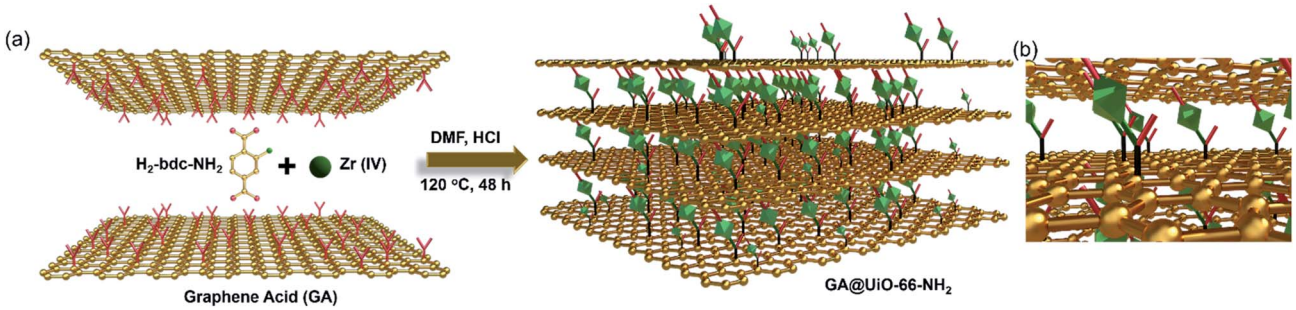

Fig. 1 (a) Schematic representation of the multifunctional (hierarchical porosity, conductive network, amine/amide functional groups) graphene–MOF hybrid (b where carboxyl groups of graphene acid are covalently linked *via* amide bonds to the amine groups of UiO-66-NH_2 MOF.

and water were also used. During the final centrifugation step with water, it was necessary to apply centrifugal force of up to 25 000 rpm to isolate the product. The resultant cyanographene was mixed with HNO_3 (65%) under stirring at room temperature. The mixture was then heated at 100 °C under reflux with stirring (350 rpm) for 24 h. Further, the product was thoroughly washed with water to remove soluble impurities to obtain graphene acid as the final material. It should be noted that, the stable aqueous suspensions of GA were prepared by adjusting the pH of the purified suspension to ~8.

2.2. Synthetic procedure for UiO-66-NH_2

Octahedral nano crystals of UiO66-NH_2 were prepared according to a slightly modified literature procedure. $ZrCl_4$ (0.233 g) and 2-aminoterepthalic acid (0.181 g)and 4-aminobenzoic acid (0.244 g) were mixed in 10 mL dimethylformamide (DMF) solvent in glass vial and dissolved by addition of 0.16 mL of hydrochloric acid (HCl). Later, the glass vial was tightly closed and placed in an oven at 120 °C for 2 days. After cooling to room temperature, the supernatant was decanted, and the pale-yellow precipitate was washed three times with DMF and three times with methanol. Methanol was decanted and replaced once per day during the course of three days and later it was removed under vacuum. The product was heated under vacuum to 150 °C for 5 h. The sample was cooled to room temperature and stored under ambient conditions.

2.3. Preparation of hybrid GA@UiO-66-NH_2

A sample of 100 mg of GA was exfoliated in 10 mL of DMF solution for 30 minutes under sonication. To this GA suspension, $ZrCl_4$ (0.233 g), 2-aminoterepthalic acid (0.181 g), 4-aminobenzoic acid (0.244 g) and 0.16 mL of HCl was added into a 25 mL glass vial. The resultant mixture was sonicated for 30 minutes. The resultant mixture was transferred to a 50 mL glass vial and placed at 120 °C for 2 days. The obtained black gel was washed several times with methanol and dried under nitrogen atmosphere at 100 °C.

2.4. Chemiresistive sensing measurement

All the materials tested for chemiresistive CO_2 sensing were weighed and pressed into pellets of uniform thickness. 150 mg of dried powdered sample were weighed and pressed with a pressure of 75 kg cm^{-2} using a hydraulic pellet press. Pellets with uniform thickness of 1 mm were obtained. Using a toothpick, small silver dots (diameter of 1 mm) were placed on the upper surface of the pellet. This silver conductive adhesive paste has a sheet resistance of <0.025 ohm $square^{-1}$ @ 0.001 mm thick. A Keithley source meter (Model no. 2450) was used to measure the resistance change in the presence and absence of CO_2 gas. The argon (reference/balance gas) and CO_2 gas flow into the gas reactor chamber were controlled by using Alicat Mass Flow Controllers (MFCs). A computer-controlled data acquisition system was used to monitor the sensor responses through the resistance-based studies. In order to carry out the sensing studies, the pellet was placed on a hollow graphite heating block containing the halogen lamp to provide the thermal energy. Argon was chosen both as reference and balancing gas. Initially, up to a desired temperature of sensing (controlled by temperature control unit), argon gas was introduced through the inlet in the gas reactor chamber. A calculated amount of CO_2 gas was injected on obtaining a stable resistance value under argon flow. The mixing chamber was used to mix the CO_2 and argon gas uniformly to obtain the desired quantity of gas flow. The resistance of the sensor/pellet was measured in presence and absence of CO_2 gas.

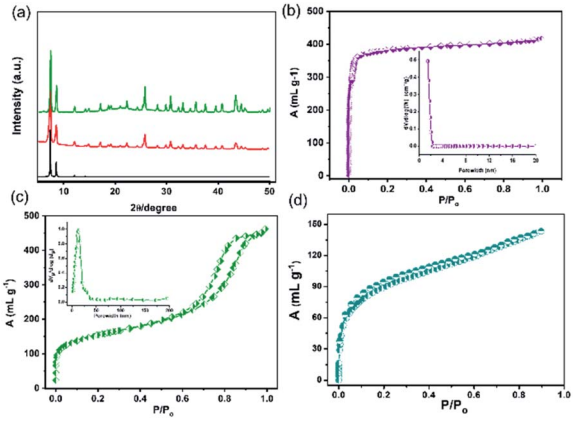

Fig. 2 (a) Simulated (black) and as synthesized powder XRD patterns of pristine UiO-66-NH_2 (red) covalent hybrid GA@UiO-66-NH_2 (green) nitrogen adsorption desorption isotherm at 77 K of (b) Uio-66-NH_2 (c) GA@UiO-66-NH_2, inset shows pore size distribution calculated through NLDFT method. (d) CO_2 adsorption isotherm measured at 195 K, for GA@UiO-66-NH_2.

3. Results and discussions

The coupling of the carboxylate functional groups of GA with pristine UiO-66-NH_2 under solvothermal conditions was done in analogy to our previously reported study.[54] The powder X-ray diffraction of the resulting hybrid (GA@UiO-66-NH_2) material confirms the structural integrity of the metal–organic framework (Fig. 2a).

Moreover, the obtained N_2 physisorption isotherm of GA@UiO-66-NH_2 features a hysteresis loop indicative of mesopores, with a Brunauer–Emmett–Teller (BET) surface area of 598 m^2 g^{-1} and a pore volume of 1.09 cm^3 g^{-1}. The pore size distribution of hybrid calculated from nonlocal density functional theory (NLDFT) method gives evidence for pores in the range from 1 to 60 nm (Fig. 2c inset). Further the Barrett, Joyner and Halenda (BJH) pore size distribution confirms meso pores in the 1–60 nm (Fig. S2a†). Contrary, pristine UiO-66-NH_2 shows microporous nature and BET surface area of 1185 m^2 g^{-1} (Fig. 2b) and NLDFT method shows micropore distribution (Inset Fig. 2b). These mesopores in GA@UiO-66-NH_2 arise from the covalent pillaring of the GA with the UiO-66-NH_2 nanocrystals. Additionally, typical features of microporous materials are observed, which originate from the intrinsic pores of the UiO-66-NH_2 nanocrystals. Furthermore, CO_2 sorption isotherms were measured GA@UiO-66-NH_2 at 195 K, and the resultant hybrid shows a significant CO_2 uptake of 157 cm^3 at $p/p_0 \sim 1$

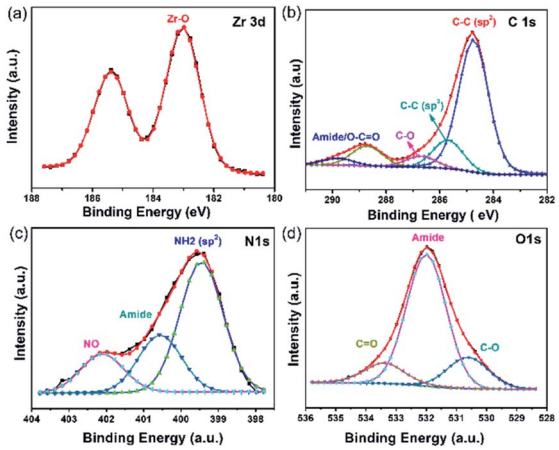

Fig. 3 Magnified XPS spectra of (a) Zr 3d (b) C 1s (c) N 1s and (d) O 1s of GA@UiO-66-NH_2.

(Fig. 2c). Further DFT pore size distribution calculated CO_2 adsorption isotherm micro–meso pore size distribution (Fig. S2b†). The deconvolution of the high resolution Zr 3d, C 1s, O 1s and N 1s from X-ray photoelectron spectroscopy (XPS) clearly reveal covalent bonds between GA and UiO-66-NH_2 nanocrystals *via* amide bond (Fig. 3a–d).[55] Scanning electron microscopy (SEM) and transmission electron microscopy (TEM) of prestine Uio-66 shows octahedron nanocrystal with size in the range of 150 to 200 nm (Fig. S1† and 4a). Finally, high-resolution transmission electron microscopy (HRTEM) images exhibit the formation of graphene nanosheets with octahedral nanocrystals between 5 to 10 nm (Fig. 4b, c, S2c and d†). Additionally, high-angle annular dark-field (HAADF) and elemental mapping from energy dispersive X-ray analysis (EDAX) shows uniform distribution of Zr, C, N, and O throughout the sample (Fig. 4d–i).

Hybridization of GA with UiO-66-NH_2 through covalent bonds yielded a hybrid system featuring electrical conductivity, hierarchical pores, amine/amide functional groups and a good CO_2 capacity, which is ideally suited for CO_2 gas sensing applications. The gas sensing measurements were carried out using a home-built two-probe gas sensing station. The two-probe method is suitable for measuring the electrical resistance of materials that have a much higher resistance than the contacts and wires used during the measurement. The probes are connected to a Keithley source meter. The gas sensing/testing chamber is equipped with a heater and gas-supplying channel that were controlled precisely by a temperature-control device and mass flow controllers (MFCs), respectively (Fig. S3†). The sensing characteristics of the material in the form of pressed pellets tested in this work include response%, response time and recovery time towards different amounts of CO_2 (100% to 5%) by recording the change in resistance *versus* time (Fig. S4†). Using the above-described setup, the resistance of pellets of GA, UiO-66-NH_2 and GA@UiO-66-NH_2 were determined, obtaining values of around 10^2 Ω, 10^9 Ω and 10^4 Ω, respectively (Fig. 5a). The low resistance of pristine GA results from the delocalized π-electrons. Nevertheless, GA do not possess any favourable interaction sites for CO_2. UiO-66-NH_2 features suitable interaction sites but has a high resistance due to the very poor orbital overlap between the Zr(IV) d-orbitals and the linker frontier orbitals. Covalent assembly of these two components leads to an intermediate resistance in the range of $\sim 10^4$ Ω which is in the range of typical metal–oxide semiconductor based sensors like SnO_2.[56]

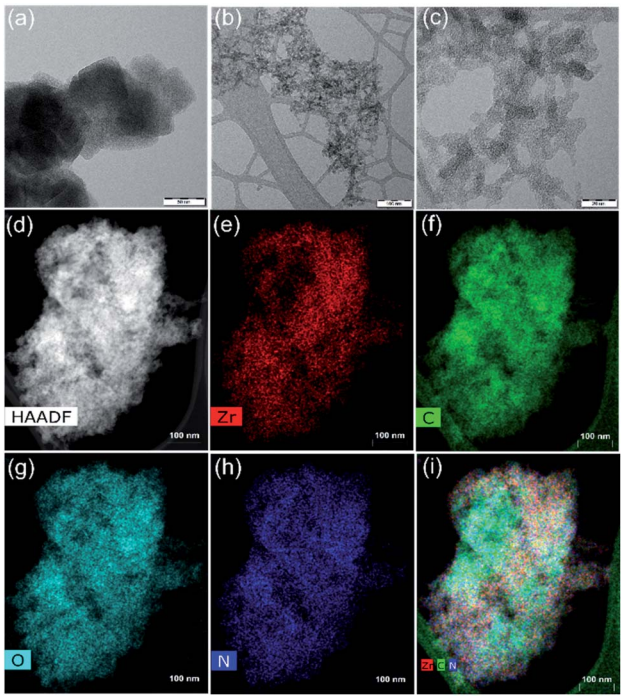

Fig. 4 HRTEM images of (a) Uio-66-NH_2 octahedron nanocrystals (b and c) GA@UiO-66-NH_2 nanocrystals of anchored graphene acid nanosheets. (d) HAADF image and elemental mapping of (e) Zr, (f) C, (g) O, (h) N, and (i) the combined distribution of Zr, C and N in GA@UiO-66-NH_2.

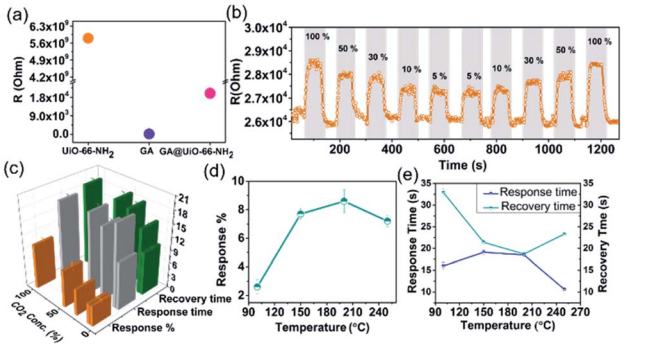

Fig. 5 (a) Comparison between the resistance of UiO-66-NH_2, GA and GA@UiO-66-NH_2, (b) gas sensing performance of GA@UiO-66-NH_2 to 5% to 100% CO_2 concentration at an operating temperature of 200 °C, (c) comparison of gas sensing characteristics (response%, response time and recovery time) from 100% to 5% CO_2 at an operating temperature of 200 °C. Effect of temperature on the sensing characteristics of GA@UiO-66-NH_2 (d) response% and (e) response and recovery times.

Based on these properties we explored GA@UiO-66-NH_2 as a CO_2 chemiresistive sensor. So far, only a handful graphene hybrids haven been reported for CO_2 sensing (Table S1†).[3,57–64] As expected, due to the lack of strong interaction sites, GA shows negligible response towards CO_2 (100% to 5%) at 200 °C (Fig. S5†). Remarkably, GA@UiO-66-NH_2 shows significant response of 10 ± 0.6% at the same temperature for 100% CO_2. For 50, 30, 10 and 5% CO_2, GA@UiO-66-NH_2 showed responses of 8 ± 0.8%, 6 ± 0.5%, 4 ± 0.2% and 4 ± 0.3% respectively, at 200 °C (Fig. 5b). The response is found to also decrease almost linearly with decrease in CO_2 concentration (Fig. S6†). The recyclability was demonstrated with three cycles of response–recovery curves (Fig. S7 and S8†). The effect of temperature on the sensing characteristics of the material is shown in Fig. 5d and e. The CO_2 response increased with increase in temperature from 2 ± 0.5% at 100 °C to 8 ± 0.8% at 200 °C for 50% CO_2. Further increase in temperature to 250 °C resulted in a slight drop in the response to 7 ± 0.4%. A very fast response and quick recovery time (~18 s) are observed at 200 °C. It should be noted that the obtained response/recovery times are either comparable or superior to other reported MOFs as shown in Table S2†.[16–19,34,36,56,65–71] The gas sensing performance of GA@UiO-66-NH_2 in presence of synthetic air is shown in Fig. S9.† The measured response% for 50% CO_2 in presence of synthetic air balance was 7%. This response% value is like the one measured in presence of argon balance gas, that is 8 ± 0.8%. The response and recovery times were in the range of 15–18 s. Hence, the effect of synthetic air was negligible on the gas sensing performance of GA@UiO-66-NH_2. For pristine UiO-66 MOF, a stable resistance of 0.5×10^{-11} Ω was measured at 200 °C under argon flow. Upon exposure to CO_2, this material did not show any detectable changes in resistance (Fig. S10†).

This could be due to the lack of strong interactive sites in the MOF. Nevertheless, the amide bridge at GA@UiO-66-NH_2 connecting the graphene basal plane and –NH_2 functionality on the pristine UiO-66-NH_2 are known to have affinity towards CO_2. The positive sensing curves (Fig. 5b) suggest that donor (amide/amine)–acceptor (CO_2) interactions led to a decrease in the conductivity of GA in the hybrid material. We rule out the possibility of sole contribution of UiO-66-NH_2 to the sensing characteristics due to its several orders of magnitude higher resistance compared to GA. It is reasonable to predict that the CO_2 interactions with the amide functionality at the interface of GA and the MOF are majorly responsible for the observed gas sensing properties (Fig. 6). The MOF has two roles in this hybrid, on one hand it controls the distance between the conductive GA layers constructing the mesoporous diffusion channels and on the other hand it provides the interaction sites at the amide functionalities at the GA–MOF interface.

Raman spectroscopy is a very useful technique to understand the interaction of gas molecules with MOFs. In order to verify the interactions proposed in Fig. 6, temperature dependent *in situ* Raman spectroscopy studies were conducted on GA@UiO-66-NH_2 in the presence of CO_2. Two new broad features appear around 1230 cm^{-1} and 1383 cm^{-1} which are assigned to adsorbed CO_2 Fermi resonance modes (Fig. S11 and enlarged figures of figure of S11 shown in Fig. S12–S18†). Dosing of Ar instead of CO_2, did not yield any new signals in this region (Fig. S19†). Variable temperature Raman spectroscopy studies were conducted in CO_2 environment from room temperature (RT) to 300 °C (Fig. 7). Fig. 7a shows the temperature dependent Raman shift of the vibrational modes corresponding to the C=O stretching, as well as the D and G bands of the GA@UiO-66-NH_2. The temperature dependent mode behaviour in Fig. 7a exhibits the expected monotonous softening (decrease in the frequency) with increase in temperature suggesting that the hybrid is stable in the temperature range of RT to 300 °C in the CO_2 environment and there is no effect of CO_2 adsorption on these modes. Fig. 7b shows the temperature dependent Raman mode behaviour of the amide (CO–NH) linkage connecting the MOF and GA, and the Fermi doublet of the CO_2 modes. Interestingly, the observed behaviour can be divided into three distinct regions (i) RT to 125 °C, (ii) 125 °C to 200 °C and (iii) above 200 °C.

The Raman modes corresponding to the amide CO–NH linkage of GA@UiO-66-NH_2 and the Fermi resonance mode of

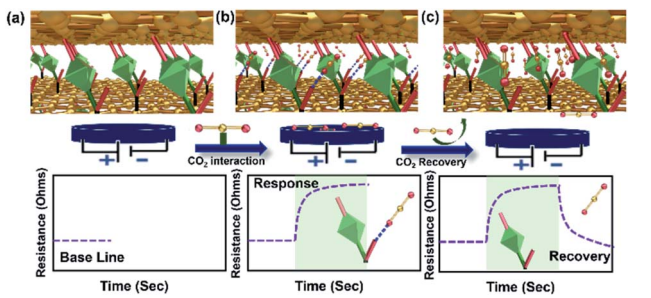

Fig. 6 Schematic illustration of possible sensing mechanism: (a) GA@UiO-66-NH_2 shows porous network with amide linkage (b) the CO_2 interactions with amide linkage present at the basal plane of the GA could bring about the positive change in resistance of GA@UiO-66-NH_2 chemiresistive sensor. (c) Upon removal of CO_2, the steady state baseline has been retrieved suggesting that CO_2 interaction is reversible.

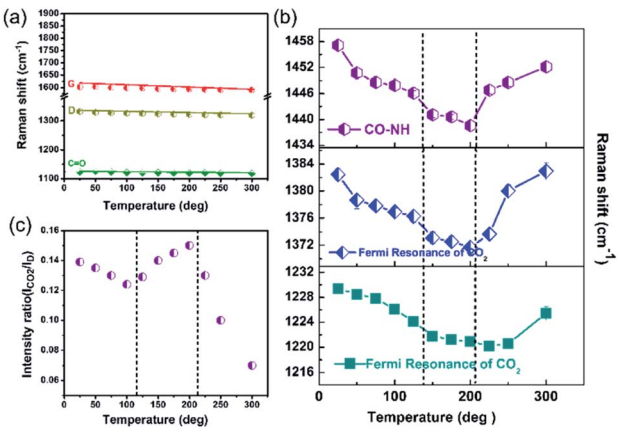

Fig. 7 Temperature dependent Raman study of GA@UiO-66-NH_2 under CO_2 atmosphere- (a) C=O stretching, D and G band, (b) CO–NH and Fermi resonance mode of CO_2. (c) Intensity ratio *vs.* temperature plot showing maximum adsorption of CO_2 around 200 °C.

CO_2 show the expected softening up to 125 °C. This suggests that there is a gradual uptake of CO_2 into the pore space without strong interactions with the walls of the pores of the hybrid with rise in temperature. Between 125 °C to 200 °C, we observe that the change in frequency shift remains nearly constant until 200 °C suggesting that further uptake of CO_2 is assisted by a strong chemical interaction between CO_2 and the CO–NH bond. We observe that above 200 °C there is a sudden increase in the frequency of both the CO–NH linkages and the two Fermi resonance modes of CO_2 and they shift back close to the values observed at room temperature. This suggests that CO_2 interacts only weakly with CO–NH above 200 °C, possibly due to the high kinetic energy associated with CO_2. This is consistent with the chemiresistive gas sensing results (Fig. 5d) where 200 °C is found to be the optimum temperature for achieving the highest CO_2 response. Further, the relative intensity ratio of CO_2 with respect to the D band ($I_{CO_2/D}$) as shown in Fig. 7c and we observe that the CO_2 intensity initially decreases up to 125 °C and then increases to a maximum intensity at 200 °C and then falls steeply beyond.

4. Conclusions

In summary, we have reported a uniquely simple, convenient, and scalable covalent assembly of graphene acid with amine functionalized UiO-66-NH_2 under solvothermal conditions. The GA@UiO-66-NH_2 hybrid acts as a chemiresistive CO_2 sensor with significant efficiency and remarkable stability. The novel CO_2 sensing characteristics might be attributed to the synergistic effect between GA and UiO-66-NH_2 in terms of good conductivity, hierarchical porous nature facilitating gas diffusion and amide/amine based interaction sites. Temperature-dependent Raman studies during CO_2 adsorption confirm interaction of CO_2 molecules with the amide bonds of GA@UiO-66-NH_2. The present data suggests a proof-of-concept for the use of this hybrid material for gas-sensing applications and there is a lot of room for the development of other conductive graphene–MOF hybrids through covalent assembly for various gas and bio-sensing applications.

Author contributions

K. Jayaramulu: idea, conceptualization, writing – original draft, super vision. M. DMello: Gas sensing measurements, writing. K. Kesavan: Raman measurments, writing – original draft. Schneemann: investigation, supervision. M. Otyepka: graphene synthesis, and investigation. S. Kment: electrochemical measurements, investigation. C. Narayna: Raman measurements and its investigation, S.Kalidindi: sensing measurements and its investigation, R. S. Varma: review & editing. R. Zboril: writing – review & editing. R. A. Fischer: writing – review & editing, super vision.

Conflicts of interest

There are no conflicts to declare.

Acknowledgements

KJR acknowledges support from Indian Institute of Technology Jammu for providing a seed grant (SGT-100038), SERB SRG/2020/000865 and CVD/2021/000086. This research was funded by the Operational Programme Research, Development and Education—European Regional Development Fund, project CZ.02.1.01/0.0/0.0/16_019/0000754 of the Ministry of Education, Youth and Sports of the Czech Republic. RZ and SK acknowledge the support from the Czech Science Foundation, project no. 19-27454X. MED acknowledges Council of Scientific & Industrial Research (CSIR), New Delhi for SRF fellowship 09/1052(0010)/2020-EMR-I) and Manipal Academy of Higher Education (MAHE) for PhD registration. MO acknowledges the ERC grant (683024) from the EU Horizon 2020 Research and Innovation Programme. the German Research Foundation (DFG) within e-conversion (Fundamentals of Energy Conversion Processes, EXC 2089) supported the work. K. K gratefully acknowledges the Department of Science and Technology for the National Post Doctoral Fellowship (PDF/2016/001193). A. S. gratefully acknowledges the Fonds der chemischen Industrie for a Liebig Fellowship.

References

1 M. Gruber, A. Trüschel and J.-O. Dalenbäck, *Energy and Buildings*, 2014, **84**, 548–556.
2 P. Puligundla, J. Jung and S. Ko, *Food Control*, 2012, **25**, 328–333.
3 A. Star, T. R. Han, V. Joshi, J. C. P. Gabriel and G. Grüner, *Adv. Mater.*, 2004, **16**, 2049–2052.
4 S. Kanaparthi and S. G. Singh, *ACS Appl. Nano Mater.*, 2019, **2**, 700–706.
5 F. H. Weinlich, *Geofluids*, 2014, **14**, 143–159.
6 X. Jia, J. Roels, R. Baets and G. Roelkens, *Sensors*, 2019, **19**, 4260.
7 N. Joshi, T. Hayasaka, Y. Liu, H. Liu, O. N. Oliveira and L. Lin, *Microchim. Acta*, 2018, **185**, 213.
8 S. Pandey, *J. Sci.: Adv. Mater. Devices*, 2016, **1**, 431–453.
9 F. L. Meng, Z. Guo and X. J. Huang, *TrAC, Trends Anal. Chem.*, 2015, **68**, 37–47.
10 D. X. Ju, H. Y. Xu, Z. W. Qiu, Z. C. Zhang, Q. Xu, J. Zhang, J. Q. Wang and B. Q. Cao, *ACS Appl. Mater. Interfaces*, 2015, **7**, 19163–19171.
11 M. G. Campbell, D. Sheberla, S. F. Liu, T. M. Swager and M. Dincă, *Angew. Chem., Int. Ed.*, 2015, **54**, 4349–4352.
12 M. G. Campbell, S. F. Liu, T. M. Swager and M. Dincă, *J. Am. Chem. Soc.*, 2015, **137**, 13780–13783.
13 D. Ju, H. Xu, Z. Qiu, J. Guo, J. Zhang and B. Cao, *Sens. Actuators, B*, 2014, **200**, 288–296.
14 F. Wang, H. Gu and T. M. Swager, *J. Am. Chem. Soc.*, 2008, **130**, 5392–5393.
15 F. I. Bohrer, A. Sharoni, C. Colesniuc, J. Park, I. K. Schuller, A. C. Kummel and W. C. Trogler, *J. Am. Chem. Soc.*, 2007, **129**, 5640–5646.
16 Y. Zhu, Y. Zhao, J. Ma, X. Cheng, J. Xie, P. Xu, H. Liu, H. Liu, H. Zhang, M. Wu, A. A. Elzatahry, A. Alghamdi, Y. Deng and D. Zhao, *J. Am. Chem. Soc.*, 2017, **139**, 10365–10373.

17 S. Pandey and K. K. Nanda, *ACS Sensors*, 2016, **1**, 55–62.
18 Y. Zhang, J. J. Kim, D. Chen, H. L. Tuller and G. C. Rutledge, *Adv. Funct. Mater.*, 2014, **24**, 4005–4014.
19 K. Saetia, J. M. Schnorr, M. M. Mannarino, S. Y. Kim, G. C. Rutledge, T. M. Swager and P. T. Hammond, *Adv. Funct. Mater.*, 2014, **24**, 492–502.
20 N. Ramgir, N. Datta, M. Kaur, S. Kailasaganapathi, A. K. Debnath, D. K. Aswal and S. K. Gupta, *Colloids Surf., A*, 2013, **439**, 101–116.
21 F. J. Ibañez and F. P. Zamborini, *Small*, 2012, **8**, 174–202.
22 B. T. Marquis and J. F. Vetelino, *Sens. Actuators, B*, 2001, **77**, 100–110.
23 Y. Zhang, B. R. Bunes, N. Wu, A. Ansari, S. Rajabali and L. Zang, *Sens. Actuators, B*, 2018, **255**, 1814–1818.
24 S. Wang, J. Liu, H. Zhao, Z. Guo, H. Xing and Y. Gao, *Inorg. Chem.*, 2018, **57**, 541–544.
25 F. Wang, Y. T. Wang, H. Yu, J. X. Chen, B. B. Gao and J. P. Lang, *Inorg. Chem.*, 2016, **55**, 9417–9423.
26 S. Mirabella, I. P. Oliveri, F. Ruffino, G. MacCarrone and S. Di Bella, *Appl. Phys. Lett.*, 2016, **109**, 143108.
27 S. F. Liu, L. C. H. Moh and T. M. Swager, *Chem. Mater.*, 2015, **27**, 3560–3563.
28 J. Hammond, B. Marquis, R. Michaels, B. Oickle, B. Segee, J. Vetelino, A. Bushway, M. E. Camire and K. Davis-Dentici, *Sens. Actuators, B*, 2002, **84**, 113–122.
29 M. D. Allendorf, R. Dong, X. Feng, S. Kaskel, D. Matoga and V. Stavila, *Chem. Rev.*, 2020, **120**, 8581–8640.
30 M. Wang, H. Shi, P. Zhang, Z. Liao, M. Wang, H. Zhong, F. Schwotzer, A. S. Nia, E. Zschech, S. Zhou, S. Kaskel, R. Dong and X. Feng, *Adv. Funct. Mater.*, 2020, **30**, 2002664.
31 H. Arora, R. Dong, T. Venanzi, J. Zscharschuch, H. Schneider, M. Helm, X. Feng, E. Cánovas and A. Erbe, *Adv. Mater.*, 2020, **32**, 1907063.
32 L. E. Kreno, K. Leong, O. K. Farha, M. Allendorf, R. P. Van Duyne and J. T. Hupp, *Chem. Rev.*, 2012, **112**, 1105–1125.
33 K. Jayaramulu, D. P. Dubal, A. Schneemann, V. Ranc, C. Perez-Reyes, J. Stráská, Š. Kment, M. Otyepka, R. A. Fischer and R. Zbořil, *Adv. Funct. Mater.*, 2019, **29**, 1902539.
34 I. Stassen, J.-H. Dou, C. Hendon and M. Dincă, *ACS Cent. Sci.*, 2019, **5**, 1425–1431.
35 C. H. Hendon, A. J. Rieth, M. D. Korzyński and M. Dincă, *ACS Cent. Sci.*, 2017, **3**, 554–563.
36 C.-W. Kung, P.-C. Han, C.-H. Chuang and K. C. W. Wu, *APL Mater.*, 2019, **7**, 110902.
37 P. Q. Liao, J. Q. Shen and J. P. Zhang, *Coord. Chem. Rev.*, 2018, **373**, 22–48.
38 Y. Wang, W. Zhang, X. Wu, C. Luo, Q. Wang, J. Li and L. Hu, *Synth. Met.*, 2017, **228**, 18–24.
39 C. W. Kung, T. H. Chang, L. Y. Chou, J. T. Hupp, O. K. Farha and K. C. Ho, *Electrochem. Commun.*, 2015, **58**, 51–56.
40 L. Zhang, Z. Su, F. Jiang, L. Yang, J. Qian, Y. Zhou, W. Li and M. Hong, *Nanoscale*, 2014, **6**, 6590–6602.
41 A. A. Talin, A. Centrone, A. C. Ford, M. E. Foster, V. Stavila, P. Haney, R. A. Kinney, V. Szalai, F. El Gabaly, H. P. Yoon, F. Léonard and M. D. Allendorf, *Science*, 2014, **343**, 66–69.
42 S. Horike, D. Umeyama and S. Kitagawa, *Acc. Chem. Res.*, 2013, **46**, 2376–2384.
43 M. D. Allendorf, A. Schwartzberg, V. Stavila and A. A. Talin, *Chem.–Eur. J.*, 2011, **17**, 11372–11388.
44 C. G. Silva, A. Corma and H. García, *J. Mater. Chem.*, 2010, **20**, 3141–3156.
45 V. Urbanová, K. Jayaramulu, A. Schneemann, Š. Kment, R. A. Fischer and R. Zbořil, *ACS Appl. Mater. Interfaces*, 2018, **10**, 41089–41097.
46 K. Jayaramulu, J. Masa, O. Tomanec, D. Peeters, V. Ranc, A. Schneemann, R. Zboril, W. Schuhmann and R. A. Fischer, *Adv. Funct. Mater.*, 2017, **27**, 1700451.
47 K. Jayaramulu, F. Geyer, M. Petr, R. Zboril, D. Vollmer and R. A. Fischer, *Adv. Mater.*, 2017, **29**, 1605307–1605312.
48 K. Jayaramulu, K. K. Datta, C. Rosler, M. Petr, M. Otyepka, R. Zboril and R. A. Fischer, *Angew. Chem., Int. Ed.*, 2016, **55**, 1178–1182.
49 J. D. Xiao, Q. Shang, Y. Xiong, Q. Zhang, Y. Luo, S. H. Yu and H. L. Jiang, *Angew. Chem., Int. Ed.*, 2016, **55**, 9389–9393.
50 H. Saleem, U. Rafique and R. P. Davies, *Microporous Mesoporous Mater.*, 2016, **221**, 238–244.
51 D. Sun, W. Liu, M. Qiu, Y. Zhang and Z. Li, *Chem. Commun.*, 2015, **51**, 2056–2059.
52 L. Shen, W. Wu, R. Liang, R. Lin and L. Wu, *Nanoscale*, 2013, **5**, 9374–9382.
53 C. Zlotea, D. Phanon, M. Mazaj, D. Heurtaux, V. Guillerm, C. Serre, P. Horcajada, T. Devic, E. Magnier, F. Cuevas, G. Férey, P. L. Llewellyn and M. Latroche, *J. Chem. Soc., Dalton Trans.*, 2011, **40**, 4879–4881.
54 K. Jayaramulu, F. Geyer, A. Schneemann, Š. Kment, M. Otyepka, R. Zboril, D. Vollmer and R. A. Fischer, *Adv. Mater.*, 2019, 1900820.
55 K. Jayaramulu, M. Horn, A. Schneemann, H. Saini, A. Bakandritsos, V. Ranc, M. Petr, V. Stavila, C. Narayana, B. Scheibe, Š. Kment, M. Otyepka, N. Motta, D. Dubal, R. Zbořil and R. A. Fischer, *Adv. Mater.*, 2021, **33**, 2004560.
56 M. E. Dmello, N. G. Sundaram and S. B. Kalidindi, *Chem.–Eur. J.*, 2018, **24**, 9220–9223.
57 K. R. Nemade and S. A. Waghuley, *Indian J. Phys.*, 2014, **88**, 577–583.
58 K. R. Nemade and S. A. Waghuley, *Int. J. Mod. Phys.: Conf. Ser.*, 2013, **22**, 380–384.
59 K. R. Nemade and S. A. Waghuley, *Opt. Mater.*, 2014, **36**, 712–716.
60 B. Andò, S. Baglio, G. Di Pasquale, A. Pollicino, S. D'Agata, C. Gugliuzzo, C. Lombardo and G. Re, *Procedia Eng.*, 2015, **120**, 628–631.
61 S. Muhammad Hafiz, R. Ritikos, T. J. Whitcher, N. Md. Razib, D. C. S. Bien, N. Chanlek, H. Nakajima, T. Saisopa, P. Songsiriritthigul, N. M. Huang and S. A. Rahman, *Sens. Actuators, B*, 2014, **193**, 692–700.
62 H. J. Yoon, D. H. Jun, J. H. Yang, Z. Zhou, S. S. Yang and M. M.-C. Cheng, *Sens. Actuators, B*, 2011, **157**, 310–313.
63 A. D. Smith, K. Elgammal, X. Fan, M. C. Lemme, A. Delin, M. Råsander, L. Bergqvist, S. Schröder, A. C. Fischer, F. Niklaus and M. Östling, *RSC Adv.*, 2017, **7**, 22329–22339.

64 K. R. Nemade and S. A. Waghuley, *J. Electron. Mater.*, 2013, **42**, 2857–2866.
65 M. G. Campbell, S. F. Liu, T. M. Swager and M. Dincă, *J. Am. Chem. Soc.*, 2015, **137**, 13780–13783.
66 M. K. Smith, K. E. Jensen, P. A. Pivak and K. A. Mirica, *Chem. Mater.*, 2016, **28**, 5264–5268.
67 M. G. Campbell, D. Sheberla, S. F. Liu, T. M. Swager and M. Dincă, *Angew. Chem., Int. Ed.*, 2015, **54**, 4349–4352.
68 M.-S. Yao, X.-J. Lv, Z.-H. Fu, W.-H. Li, W.-H. Deng, G.-D. Wu and G. Xu, *Angew. Chem., Int. Ed.*, 2017, **56**, 16510–16514.
69 M. E. Dmello, N. G. Sundaram, A. Singh, A. K. Singh and S. B. Kalidindi, *Chem. Commun.*, 2019, **55**, 349–352.
70 E.-X. Chen, H.-R. Fu, R. Lin, Y.-X. Tan and J. Zhang, *ACS Appl. Mater. Interfaces*, 2014, **6**, 22871–22875.
71 E.-X. Chen, H. Yang and J. Zhang, *Inorg. Chem.*, 2014, **53**, 5411–5413.